

Nanoscale

Accepted Manuscript



This is an *Accepted Manuscript*, which has been through the Royal Society of Chemistry peer review process and has been accepted for publication.

Accepted Manuscripts are published online shortly after acceptance, before technical editing, formatting and proof reading. Using this free service, authors can make their results available to the community, in citable form, before we publish the edited article. We will replace this *Accepted Manuscript* with the edited and formatted *Advance Article* as soon as it is available.

You can find more information about *Accepted Manuscripts* in the [Information for Authors](#).

Please note that technical editing may introduce minor changes to the text and/or graphics, which may alter content. The journal's standard [Terms & Conditions](#) and the [Ethical guidelines](#) still apply. In no event shall the Royal Society of Chemistry be held responsible for any errors or omissions in this *Accepted Manuscript* or any consequences arising from the use of any information it contains.

ARTICLE

Nanohelices by shadow growth[†]

Cite this: DOI: 10.1039/x0xx00000x

John G. Gibbs,^a Andrew G. Mark,^a Tung-Chun Lee,^a Sahand Eslami,^a Debora Schamel,^a and Peer Fischer^{*a,b}Received 00th January 2012,
Accepted 00th January 2012

DOI: 10.1039/x0xx00000x

www.rsc.org/

The helix has remarkable qualities and is prevalent in many fields including mathematics, physics, chemistry, and biology. This shape, which is chiral by nature, is ubiquitous in biology with perhaps the most famous example being DNA. Other naturally occurring helices are common at the nanoscale in the form of protein secondary structures and in various macromolecules. Nanoscale helices exhibit a wide range of interesting mechanical, optical, and electrical properties which can be intentionally engineered into the structure by choosing the correct morphology and material. As technology advances, these fabrication parameters can be fine-tuned and matched to the application of interest. Herein, we focus on the fabrication and properties of nanohelices grown by a dynamic shadowing growth method combined with fast wafer-scale substrate patterning which has a number of distinct advantages. We review the fabrication methodology and provide several examples that illustrate the generality and utility of nanohelices shadow-grown on nanopatterns.

1 Introduction

Helical architectures play an important role in science and technology. For example, electrical current traversing a helical path, such as in a solenoid, produces a magnetic field along the helix axis. In electronics, an inductor is a fundamental component which resists changes in electrical current thus imparting impedance to the circuit. Helical antennas¹ typically receive or emit radio frequency radiation in which the antenna pitch is significantly smaller than the wavelength of the radiation. To realize an analogous helical visible light antenna,² the necessary dimensions of the helix would have to be roughly an order of magnitude smaller than the wavelength of visible light, i.e. tens of nanometres, a technological challenge, yet the fabrication scheme we highlight in this article is able to produce nanohelices with these dimensions.

The helix is found at the nanoscale primarily within biological molecules. For example, the α -helix, a coiled conformation, is one of the most common secondary structures of proteins.³⁻⁵ Perhaps the most famous example is the DNA double helix, whose structure was first unravelled by Watson and Crick in 1953.⁶ Knowing that the helix morphology is necessary for these bio-molecules to be functionally viable, an important question to ask is: can desired properties of materials be introduced by engineering artificial nanomaterials with this morphology? If control over the critical dimensions of the helix as well as the material composition can be achieved, then we hope to show here that the answer is yes.

Recent fabrication advances have made it possible to produce a wide range of helical morphologies from a variety of different materials. Excellent reviews about the state of the art until about 2011 can be found in the following references.^{7, 8} In this article, we review a more recent fabrication advance that can be used to grow some of the smallest and most versatile

nanohelices. Herein, we implement a dynamic fabrication method that makes it possible to grow nanostructures, including nanohelices, with programmable 3D features from a wide range of different materials, including hybrids and composites. We discuss structures that have been grown in particular for this article and that have not been published previously; including designed conical nanohelices with a controlled increase in the helix major radius, alloyed plasmonic nanohelices that have tuned resonances in the visible, as well as magnetic nanohelices that are < 50 nm in total length, to name but a few.

Representative examples of some micro- and nano-helices grown by other methods as well as the method of this review are shown in Figure 1, although this is by no means an exhaustive list. Figure 1 (A) shows scanning electron microscopy (SEM) images of nanohelices formed from zinc oxide nanobelts grown via a vapour-solid growth process, which owing to the piezoelectric properties of ZnO, could have applications in sensors and transducers.⁹ Figure 1(B) shows ZnS semiconductor helical nanotubes produced by supramolecular self-assembly.¹⁰ Self-assembly of a biocoordination polymer into nanobelts has been demonstrated as well (not shown here).¹¹ The example in Fig. 1(C) shows the fabrication scheme and resultant images of Pd nanohelices, which when a magnetic section of Ni is added, can be driven by a rotating external magnetic field.¹² The fabrication method in Fig. 1(C) is a template-based electrodeposition set-up and produces uniform helices in parallel.¹³ Figure 1(D) shows transmission electron micrographs (TEM) of several nanohelices fabricated by confined assembly of silica-copolymer mesostructures formed in alumina nanochannels.¹⁴ DNA self-assembly was used to produce structures of helically-arranged Au nanodots as shown in the TEM image of Fig. 1(E).¹⁵ The plasmonic coupling of the Au nanodots in this case leads to enhanced chiroptical effects. Figure 1(F) shows

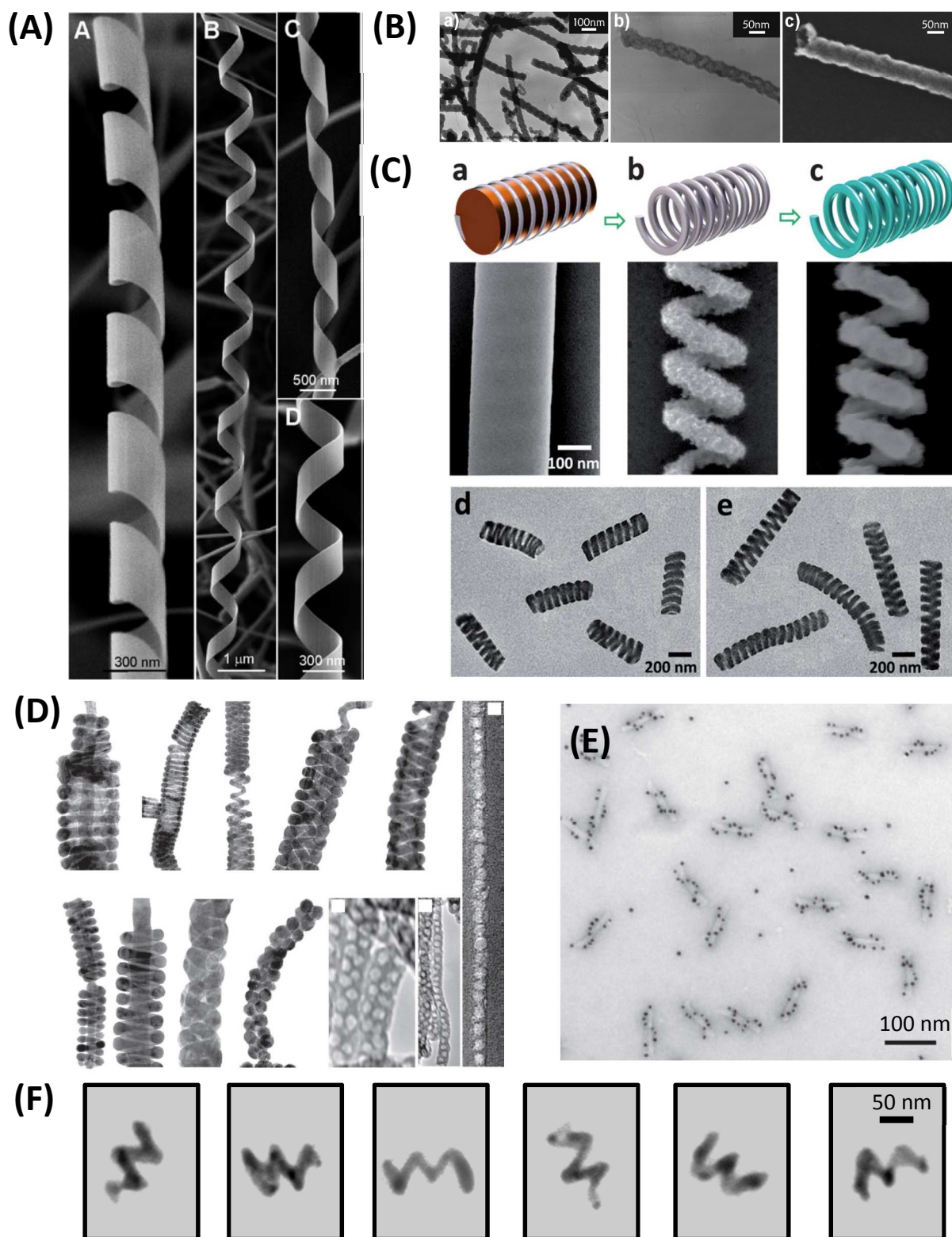


Fig. 1 Examples of nanohelices in the literature: **(A)** zinc oxide helical nanobelts, reprinted with permissions from Ref. 9; **(B)** ZnS semiconductor helical nanotubes, reprint from Ref. 10; **(C)** Pd nanohelices, reproduced from Ref. 11 with permission from The Royal Society of Chemistry; **(D)** silica-copolymer mesostructures grown in confined nanochannels of (from top left to bottom right): 64, 64, 62, 51, 45, 41, 40, 31, 28, 28, 18, 18 nm, respectively, reprint from Ref 13; **(E)** helically arranged Au nanodots by DNA self-assembly, reprint from Ref. 14; and **(F)** Cu nanohelices formed by dynamic physical vapour deposition combined with micelle lithography (focus of this article).

TEM images of individual Cu nanohelices fabricated by dynamic physical vapour deposition coupled with micellar lithography that is the focus of this article.¹⁶ With this method, control over the helix critical dimensions, including the helix pitch, number of turns, major and minor radius, and the material composition gives it advantages over many other methods. Examples of material that can be used include but are not limited to metals, semiconductors, magnetic materials, metal oxides, and combinations of these. Fabrication, applications and physical properties of nanohelices produced with this technique will now be discussed in turn.

2 Dynamic physical vapour deposition

A physical vapour deposition technique termed glancing angle deposition (GLAD)¹⁷⁻²¹ allows for the fabrication of helical structures. This method relies upon the shadowing effect.²² When physical vapour impinges upon a substrate at an

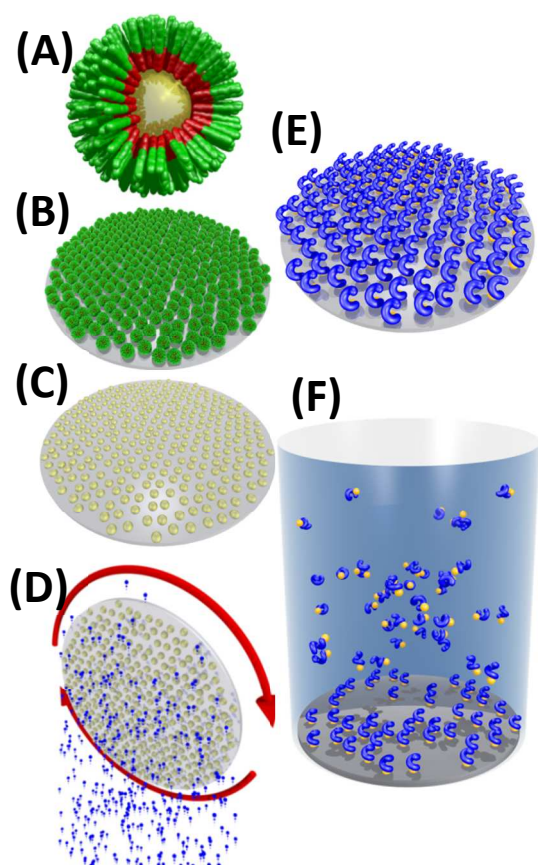


Fig 2 Schematic of block copolymer micelle lithography (BCML) combined with oblique angle deposition process to produce colloidal nanohelices as explained in the text.

oblique angle, arrays of columns form on the surface; when the substrate is slowly rotated, then helices are formed. The rotation rate of the substrate holder during deposition determines the pitch of the helix.

Also, if the substrate is seeded, growth of the material can be restricted to the seeding points. The size and spacing of the seeds affects the final morphology of the helix. GLAD has long been used to fabricate porous thin films with roughly micron-sized features. Nanoscale features in GLAD films are

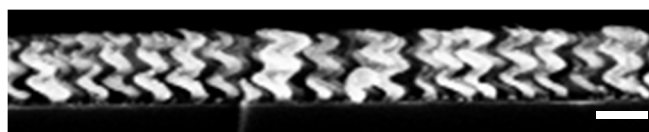


Fig. 3 Cross sectional SEM image of Ag/Cu 50:50 alloy nanohelices grown using BCML seeded shadow growth (view of the wafer-edge). Scale bar = 100 nm.

possible through substrates seeded using e-beam lithography,^{23, 24} but due to the slow write times involved, fast, wafer-scale processing is not possible with this method. We overcome this limitation by using a rapid lithography process.

We have recently shown that the critical dimensions of nanohelices may be reduced and that the types of materials may be extended by controlling the seed dimension and using an efficient lithography process.¹⁶ Not only do the small dimensions of the seeds translate to small feature sizes, the regular spacing leads to greater morphological uniformity between individual structures. The schematic in Figure 2 shows dynamic oblique angle deposition combined with block copolymer micelle lithography (BCML). Figure 2(A) shows a diblock copolymer surrounding an Au nanoparticle. The micelles are deposited as a monolayer by spin-coating onto a clean flat surface as shown in Fig. 2(B). Plasma etching removes the polymer leaving behind the Au (or other metals) nanoparticles which are arranged in a hexagonal manner, as shown in Fig. 2(C), with the separation between individual Au nanodots determined by the length of the diblock. The patterned surface, which is usually a Si or SiO₂ wafer, is then introduced to a vacuum chamber and tilted to an oblique angle with respect to the incident vapour. Material is vaporized by ebeam heating and the vapour deposits onto the surface of the substrate. Shadow growth from the oblique angle leads to nanoscale

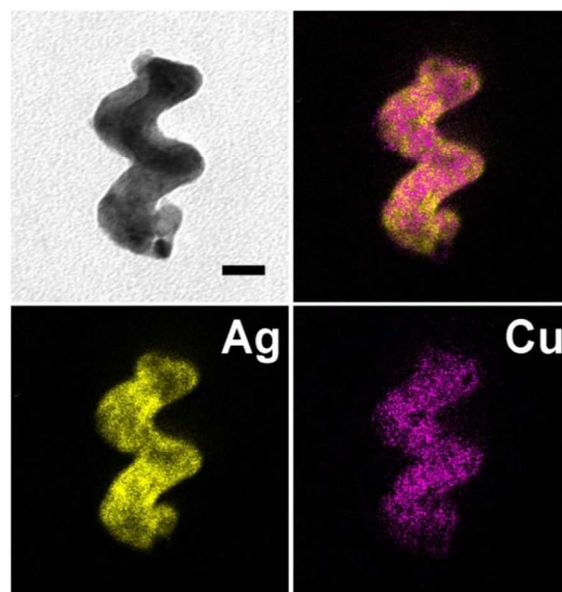


Fig. 4 Energy-filtered TEM (EF TEM) chemical mapping of a Ag/Cu alloy nanohelix showing the distribution of each element. Zero-loss EF TEM image (top left). False-colour elemental maps of silver (bottom left) and copper (bottom right) generated using the three-window technique. Overlay of the Ag and Cu channels (top right) showing nanoscale alloying. Colour code (and corresponding core-loss edges): yellow, silver (Ag M_{4,5}); purple, copper (Cu L_{2,3}). Scale bar = 20 nm.

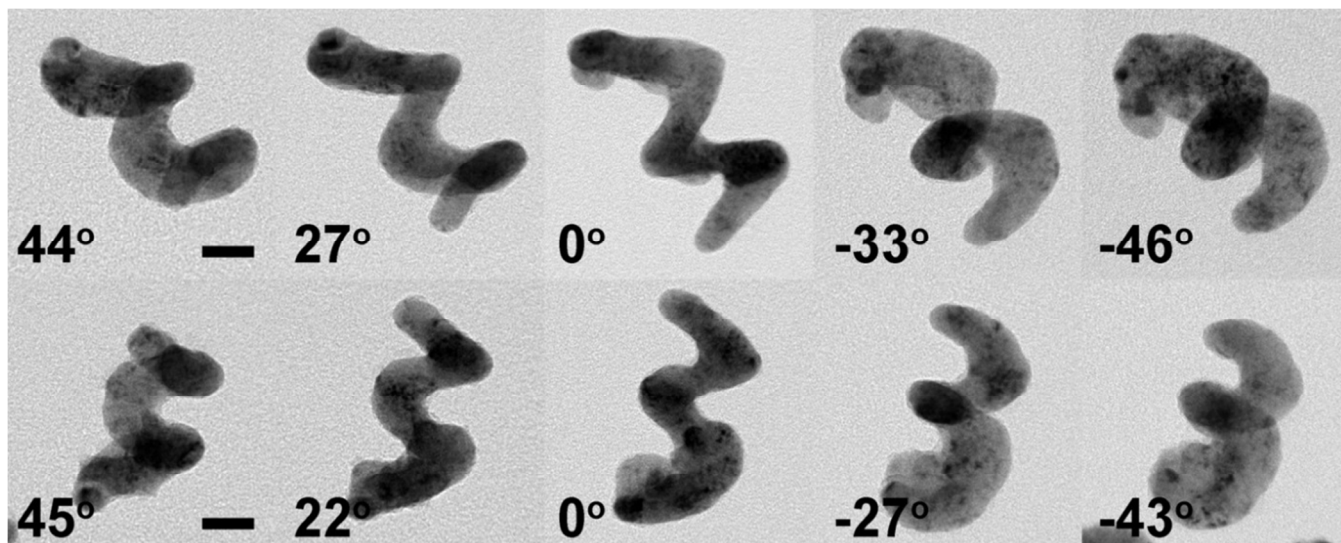


Fig. 5 TEM images of two typical Ag/Cu alloy nanohelices (top and bottom) at various tilt angles. Scale bar = 20 nm.

columnar growth onto the seeds. The tilt angle and rotation speed of the substrate (holder) are dynamically controlled in real time during the deposition process. The rotation of the substrate is represented by the red arrows in Fig. 2(D). Figure 2(E) shows a schematic of a 1-turn helix array which forms after a single rotation of the substrate during deposition. The helix pitch is determined by the ratio of the deposition rate to the rotation rate. Many applications call for aligned and arranged helices as in Fig. 2(E). However, for applications that require individual helices or for helices suspended as a colloidal solution, the substrate supporting the helices can be sonicated in a liquid (e.g. H₂O), which detaches the structures from the surface, as depicted in Fig. 2(F). The cross-section SEM image of Fig. 3 shows a representative Ag/Cu alloy nanohelix array with 2 turns (prior to sonication), in analogy to Fig. 2(E). The TEM images of Fig. 1(F) show individual Cu nanohelices, which have been removed from the surface by sonication as schematically shown in Fig. 2(F).

The two important parameters are φ and α which are the substrate rotation and vapour incidence angles, respectively. If the substrate rotation rate $d\varphi/dt = 0$, and the deposition angle α is oblique, $0^\circ < \alpha < 90^\circ$, the surface area of the deposited material increases and the film becomes porous. As α approaches 90° , separated nano-columns begin to form; this effect occurs even on a perfectly flat surface due to random nucleation of material which serve as points of growth and subsequently shadow their neighbours. The tilt angle of the columns, β , can be approximated by the empirically derived formula²⁵

$$\tan \alpha = 2 \tan \beta \quad (1)$$

which is a first-order approximation for angles which are not too close to $\alpha = 90^\circ$. As α approaches 90° , a correction is made to the tilt angle²⁶

$$\beta = \alpha - \arcsin\left(\frac{1}{2} - \frac{1}{2} \cos \alpha\right) \quad (2)$$

which is also an approximation. It should be noted that the contributions to the tilt angle are many with the most important being the type of material which is being deposited. The

formation of helices is achieved by simply rotating the substrate during deposition at some fixed ratio of material thickness to substrate rotation angle, φ . In this manner, the helix pitch and height can be controlled.

The final morphology is also highly material dependent. With materials such as oxides and some semiconductors, the final shape varies usually only negligibly with temperature. With other materials such as pure metals, in particular Au and Ag, the relatively high room temperature surface diffusion of the adatoms, i.e. the atoms which are accumulating at the ends of the structures, leads to poor formation. Because the surface diffusion of adatoms is temperature dependent, it follows that reducing the substrate temperature significantly aids the controlled formation of complex shapes.

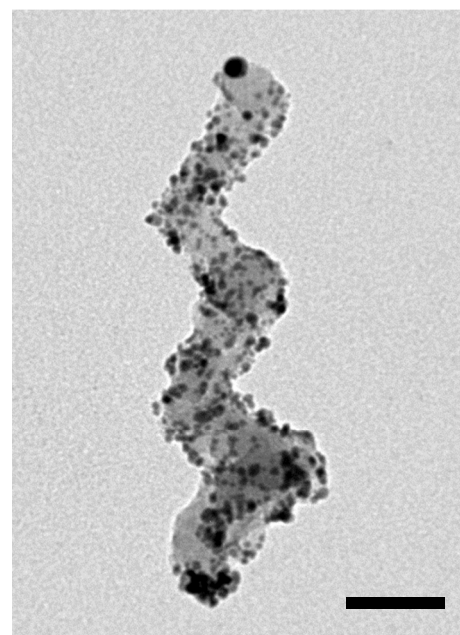


Fig. 6 TEM Au-nanoparticle-decorated SiO₂ nanohelix. Scale bar = 50 nm.

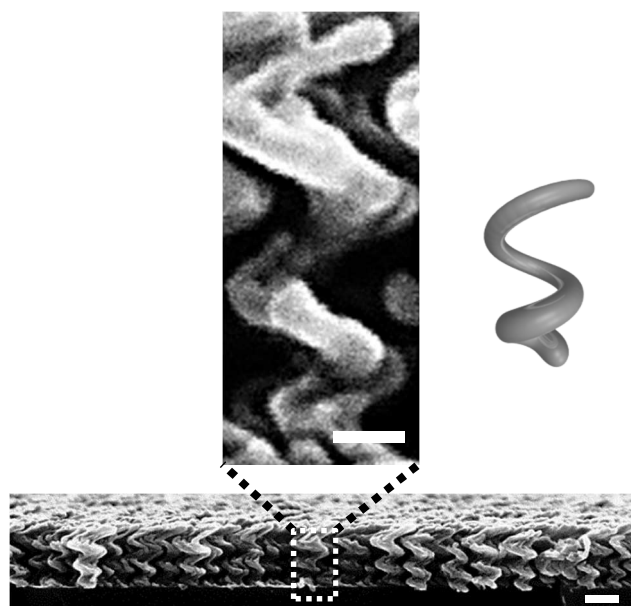


Fig. 7 SEM cross-section image of an array of Cu conical helices. Scale bar =100 nm; top: zoomed-in SEM image of a single Cu conical nanohelix. Scale 25 nm; right: schematic representation of a conical helix.

Once the atom or molecule has landed on a forming column, it diffuses across the surface both directionally and randomly due to the substrate tilt angle, and these effects become increasingly important at the nanoscale. The directional diffusion is a result of the kinetic energy which the adsorbing species possess leading to changes in the column tilt angle with respect to the substrate normal,²⁷ while random diffusion is non-directional and is characterized by hopping between adjacent adsorption sites at a rate given by $\Gamma = \nu e^{-E/k_B T}$, where E is the energy barrier to diffusion and ν is the attempt frequency of the adatom. In reality, the diffusion of adatoms is much more complex than this simplified model suggests.²⁸ Temperature is not the only parameter affecting the final morphology of structures formed at oblique incidence, but one must also consider the crystal properties of the material, the relative angle between the vapour plume with respect to crystal axes,^{29, 30} deposition and burial rates, as well as contamination from residual gas adsorption. In this manner, simply decreasing the temperature is often not sufficient to improve the quality of the helices as we have found in the case for pure Ag. A systematic study is required to further illuminate the coupling between these various effects, and this is beyond the scope of this article. Nevertheless, we do find that with certain metals, simply lowering the substrate temperature does increase the fidelity of our helices such as the Ag/Cu alloy shown in Figs. (3), (4) and (5) which do improve with substrate temperature reduction. It should be noted that very recently, high quality Ag/Ti helices can be fabricated at room temperatures as well,³¹ showing the importance of alloying. The SiO₂ backbone in Fig. 6 does not require cooling of the substrate as the surface diffusion is presumably already quite low.

3 Examples

To illustrate the versatility of the fabrication technique, we now illustrate four examples of nanohelices with different morphologies and material composition. By co-depositing two

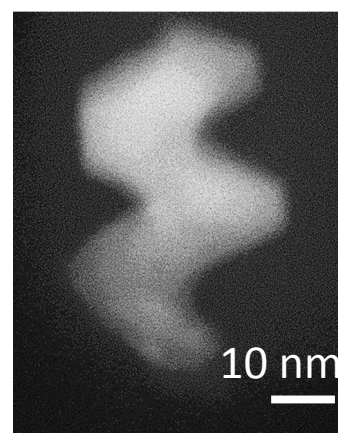


Fig. 8 HAADF STEM image of the smallest nanohelix grown by this method to date. The material is Ni and it has a length of ~ 50 nm.

metals simultaneously, it is possible to form alloyed nanohelices. The top-left panel of Fig. 4 shows a zero-loss energy-filtered TEM (EF TEM) image of a two-turn Ag/Cu alloy nanohelix. The materials were co-deposited to yield 50:50 alloys. The ratio of the two deposition rates is held constant to maintain the intended material composition. The top-right panel of Fig. 4 shows the elemental map for Ag and Cu, which are also shown individually in the bottom-left and bottom right panels of Fig. 4, respectively. Qualitatively, it is seen that each element is distributed fairly evenly throughout the nanohelix suggesting a homogenous composite or nanoscale alloying. In order to show the geometry of an individual nanohelix, which is in this case the same sample as the one shown in Fig. 4, TEM images were recorded under various tilt angles for two typical Ag/Cu nanohelices which are shown in Fig 5, clearly illustrating the 3-D helical morphology.

The next example we discuss is shown in the TEM image of Fig. 6. The backbone of the helix is grown from SiO₂. The nanohelix is further processed after the deposition procedure described in Fig. 2 in order to decorate the surface with ~5 nm gold nanoparticles (Au NPs) that are coupled to the surface of the glass nanohelix. The Au NPs are attached by on-wafer chemical functionalization with a thiol-silane, followed by incubation of the functionalized surface in an aqueous solution of 5-nm Au NPs. It has been shown recently that similar morphologies can be fabricated by physical vapour deposition alone.³² Such structures are analogous to the DNA-assembled Au nanoparticles as in Fig. 1(E), and therefore may be useful for chiral plasmonic applications. For example, giant enantiomeric sensing has recently been shown as a result of plasmonic coupling of nanoparticles arranged on a chiral structure.³³

Next, we present a conically shaped nanohelix which cannot, to the best of our knowledge, be fabricated via any other method. We have shown recently that for this fabrication method the relationship between the helix pitch, P , and the helix major radius, a are related by the following $a \propto 0.3P$.³⁴ It follows, that if the relationship between the deposition rate and the rotation rate is varied, the helix diameter can be controlled

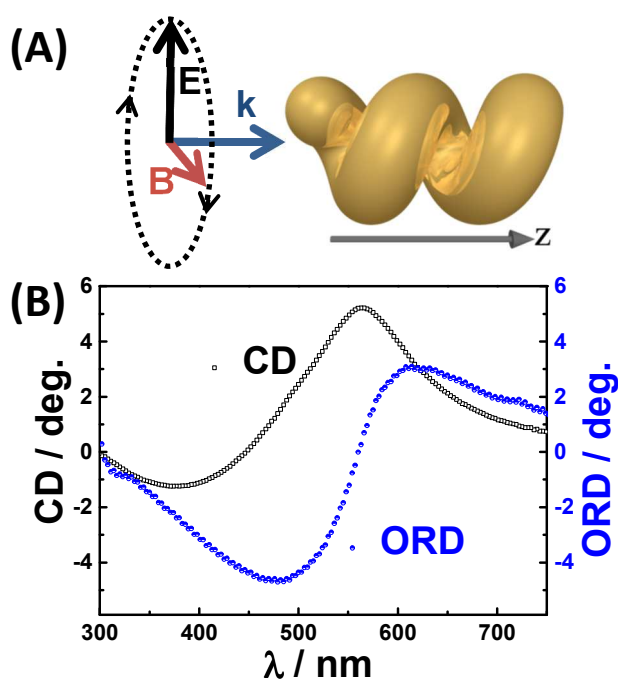


Fig. 9(A) schematic of circularly polarized light propagating along the axis of the helix; (B) relationship between circular dichroism and optical rotatory dispersion for an array of Ag/Cu plasmonic nanohelices.

during growth to yield a conically-shaped helix. This structure could have uses in such applications as a broadband helical antenna³⁵ or, for mechanical applications, as a conical helix exhibits a non-linear spring constant. Helix bundling has been shown to give a non-linear response to mechanical stress at the nanoscale, but those helices had uniform pitch and major radius.³⁶ The responses of applied forces on non-conical, micron-sized springs fabricated by GLAD have been studied previously.³⁷ Figure 7 shows a representative SEM image of a Cu conical helix (on the substrate surface). The conical shape is formed by slowly decreasing the ratio of the rotation rate to deposition rate. It can be seen that the helix pitch and major radius are both larger at the top in comparison to the bottom. For each half turn shown in the SEM image of Fig. 7, the major radius changes from $a = 20.5, 26.8, 34.8, 37.5, 44.6$ nm from bottom to the top.

The last example showcases the smallest artificial nanohelix fabricated to date. The high-angle annular dark-field scanning transmission electron microscopy (HAADF STEM) image shown in Fig. 8 shows a Ni nanohelix which is ~ 50 nm in total length with a helix pitch of ~ 25 nm.

4 Properties and applications

A helix has chiral (no mirror-image) symmetry. The two mirror-image forms of the helix are known as enantiomorphs. This symmetry breaking can be exploited in optical or mechanical applications. For instance, the coupling of rotation of the helix about the helix axis can cause translation, as in a screw or propeller. At small length-scales in liquids, it is necessary to have a non-reciprocal motion in order to gain

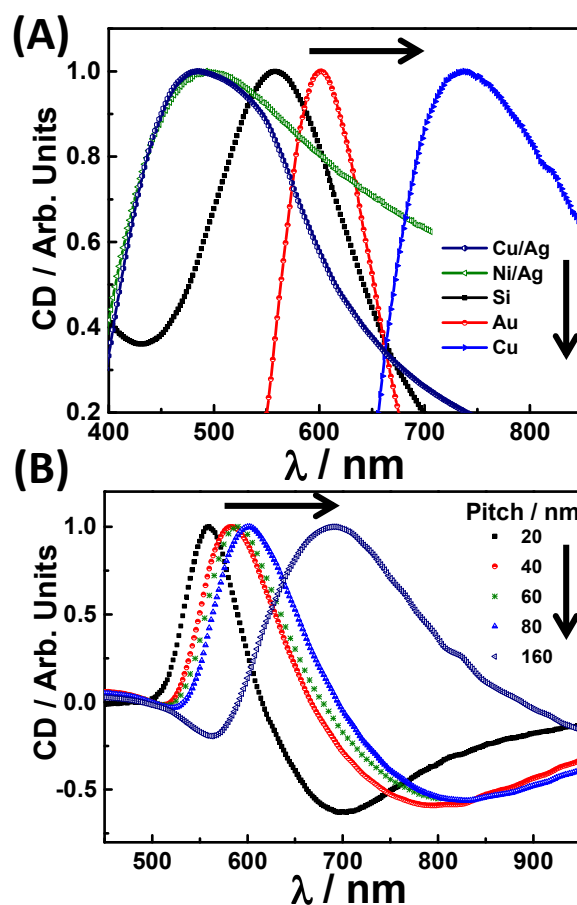


Fig. 10(A) CD spectra for 5 different materials in a nanohelix array supported by a glass (transparent) substrate: Cu/Ag and Ni/Ag alloys, and Si, Au, and Cu pure materials; (B) normalized CD spectral peaks for various Au nanohelix colloidal suspensions (in a 1 cm path length cuvette) with various pitch ranging from 40, 50, 60, 80, 160 nm. The trend in the graph shows a red-shift corresponding directly to the size of the helix pitch. The arrows in (A) and (B) relate the spectra to each sample in the legend.

controlled mobility due to hydrodynamics at low Reynolds number.³⁸ The helix naturally fulfils this requirement. We will discuss the magnetic actuation and locomotion of helices in sections 4.2 and 4.3, but first turn our attention to the optical properties of the helix.

4.1 Optical properties

A nanohelix interacts preferentially with circularly polarized light, giving rise to optical rotation (OR), and the differential absorption of circularly polarized light, known as circular dichroism (CD). Unlike molecules, optical activity phenomena can be orders of magnitude stronger in engineered nanostructures. Since linear optical activity phenomena involve higher-order multipolar light-matter interactions it follows that when the structure is of the order of the wavelength of light, then these effects can become large. Use of metals that exhibit collective surface electron-oscillations, known as surface plasmons, can further enhance the electromagnetic fields

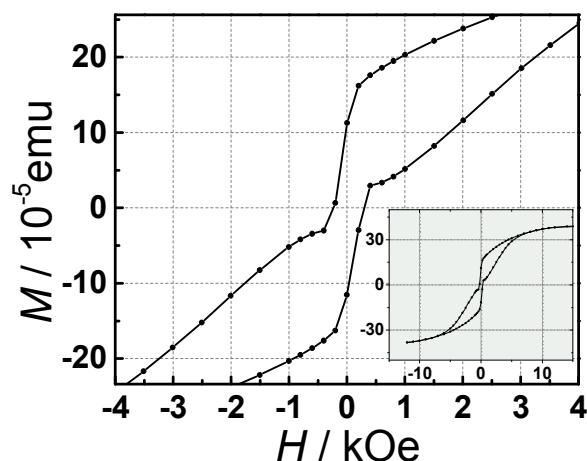


Fig. 11 Hysteresis curve, measured by SQUID, for a 1.5-turn, left-handed, Co nanohelix array with total height of ~ 230 nm.

around a plasmonic nanostructure, which may give rise to especially large optical activities. The combination of chirality and plasmonics is known as chiral plasmonics.^{15, 34, 39-41} An exciting possibility is that optically active (chiral) nanostructures could be used to realize a metamaterial with a negative index of refraction.⁴² For this particularly large optical activities are needed. Fig. 9(A) shows a schematic of circularly polarized light impinging upon a plasmonic nanohelix. Due to its chirality, one polarization state is absorbed/scattered more than the other (CD). CD is shown in degrees of ellipticity where $\tan \theta = (|E_{RCP}| - |E_{LCP}|) / (|E_{RCP}| + |E_{LCP}|)$ in which E_{RCP} , E_{LCP} are the electric field components of RCP and LCP, respectively. Dichroism involves the imaginary part of the refractive index, while optical rotation is related to the real part. Fig. 9(B) shows the relationship of CD and OR for an example nanohelix array grown using the shadow growth method of this paper.

The resonance wavelength of a nanohelix is a function of both the material from which the nanohelices are made¹⁶ as well as the critical dimensions of the helix.³⁴ We have shown recently that the chiroptical spectral peak position is different for Au, Cu, and Cu/Ag alloy nanohelices (in a colloidal suspension).¹⁶ Fig. 10(A) shows the normalized CD peaks of nanohelices that have the same pitch $P \sim 50$ nm but that are respectively made from Au, Cu, and Si, as well as two alloys Cu/Ag and Ni/Ag of 50:50 atomic ratio. The morphology of all five samples is nearly identical, as the growth conditions were kept constant for each deposition. The well-separated peaks demonstrate how material composition can be used to tune the chiroptical response. By depositing multiple materials simultaneously, we achieve alloyed nanohelices, like the ones in Fig. 4 and Fig. 5, which show resonances dependent upon the stoichiometry of the alloy. Alloying of Cu with Ag for instance blue-shifts the resonance from 750 nm to 470 nm. However, the plasmonic response of an alloy is not simply given by the average of the constituent materials' dielectric constants,⁴³ as can be seen in the case of the Ni/Ag and Cu/Ag alloys. In this manner, we can tune the resonant wavelengths to cover the



Fig. 12 SEM cross-section image of small magnetic swimmers. Contrast in image clearly shows location of magnetic Ni section (light color). Scale bar 100 nm.

entire visible spectral range simply by changing the material composition.

As we have recently demonstrated, the morphology of the helix is important in determining the position of the resonance as well.³⁴ Figure 10 (B) shows that the resonance position is also a function of the dimensions of the helix. Normalized CD spectral peaks for various Au nanohelix colloidal suspensions with various pitches ranging from 40, 50, 60, 80, 160 nm are shown. The trend in the graph shows a red-shift corresponding directly to the size of the helix pitch. Since these samples are colloidal suspensions, Au was chosen due to its stability in H_2O . In order to suppress aggregation, the nanohelices are suspended in a dilute (1mM) solution of sodium citrate. These colloidal metafluids could be used for ultrasensitive detection of chiral molecules.^{40, 44-46}

4.2 Magnetic properties

The versatility of the growth method also permits the formation of magnetic nanohelices. Since shape anisotropy plays an important role in determining magnetic alignment, it follows that controlled variation of nanohelices' structural parameters can be used to tailor their magnetic properties. Some examples of magnetic GLAD-grown structures have been shown previously,⁴⁷ such as periodic magnetic microstructures, including helices,⁴⁸ as well as Si/Ni springs.⁴⁹ Here we show that nanohelices of pure Co show magnetic hysteresis, demonstrating that they retain their ferromagnetism even at this scale.

The large graph of Fig. 11 shows the magnified centre portion of the hysteresis curve for clarity, while the inset shows the curve in its entirety. In this case, the magnetic response of Co helices is measured at room temperature on the substrate with a superconducting quantum interference device (SQUID). The helices are ~ 180 nm long and have a helix pitch of $P = 90$ nm. The saturation magnetisation is 6.3×10^5 A/m which gives a saturation magnetic field of 0.8 T. This compares favourably with the saturation polarisation of 1.7 T for bulk Co and the value of 1.6 T reported in a recent work based on Lorentz TEM mapping of Co nanohelices.⁵⁰ Two factors may contribute to the lower magnetization measured here: first, Petford-Long et al. found that the local magnetisation follows the sweep of the helix. This will lead to an undetectable transverse component to the magnetisation. Correcting for this means that locally the fields in our helices could be as high as 1.1 T. Furthermore, in the same study, "antiferromagnetic"-type alignment between

the magnetizations of adjacent helices was observed. In the far field this will also serve to reduce the observed magnetisation. The discontinuities of the hysteresis curve in Fig. 11 are possibly due to shape anisotropy⁵¹ of the nanohelices and possible vortex formation,⁵² although we are not claiming to substantiate these hypotheses here.

4.3 Magnetic nano-propellers

Propulsion of artificial micro- and nanostructures is difficult due to thermal, or Brownian, fluctuations as well as the hydrodynamic conditions encountered at low Reynolds number, where viscosity dominates over inertial effects.³⁸ At low Reynolds number, it is therefore necessary for a natural biological swimmer or an artificial micro or nano-propeller to undergo non-reciprocal motions in order to gain directed mobility. It should be noted that reciprocal motion can enhance diffusion, but in this case the motion is completely random.^{53, 54} A helix rotating about its axis in one direction fulfils the non-reciprocity requirement. As the helical structure rotates, coupling between the particle and the viscous fluid propels it forward translationally. It has recently been shown that externally driven nano-propellers can be fabricated with GLAD.^{55, 56} Because a ferromagnetic section can easily be added to the helical structure, the nano-propellers can be driven by an external rotating homogeneous magnetic field. An application has been shown recently in which a racemic mixture of left and right handed nano-propellers will separate under the influence of the same field, i.e. chiral separation.⁵⁷

An array of nano-propellers (on the substrate) is shown in the cross-section SEM image of Fig. 12. The initial seed layer in this case is a monolayer of SiO₂ nanobeads of ~75 nm diameter deposited with a Langmuir-Blodgett trough, and the helical section is also formed of SiO₂. The total length of the combined structure is ~450 nm. From the micrograph, it is easy to see the magnetic Ni section as the bright segment just above the nanobeads onto which the screw propellers are grown. The Ni section allows for the magnetization of the structure. Switching between materials is quite simple, and hybrid structures such as this one can be readily produced. These helices are several times larger than the other examples in the article but for good reason. As a propeller becomes smaller, it becomes more difficult to control the motion due to thermal fluctuations.⁵⁸ The rotational diffusion constant, i.e. the average time it takes for the particle to reorient itself, scales as $1/r^3$, in which r is the characteristic length of the particle. Although controlled propulsion at the nanoscale is challenging, a number of interesting applications could be possible such as probing the intracellular matrix of cells or other complex fluids which have features on a similar scale.

It has been suggested that robots on the micro- to millimetre scale could be used for promising non-invasive medical applications such as biopsies and targeted delivery,⁵⁹ although this field is still in its infancy. Scaling down the size of this type of robotics suggests ways to navigate complex biological tissues and possibly the interior of cells. A first step toward

biomedical applications at the nanoscale is therefore to understand the physics of nano-propellers in biological fluids. In particular, micro- and nano-rheology of complex biological fluids can be studied using magnetic nano-propellers. Many biological fluids consist of polymeric networks that have distinctive mesh sizes in the range of tens to hundreds of nanometres, and display strongly size-dependent transport behaviour.⁶⁰⁻⁶³ A fundamental understanding of how nano-propellers move in such environments may pave the way for targeted operation inside living tissue which almost always consists of such materials.

5 Conclusions

In this article we have focused upon a versatile fabrication technique which combines glancing angle deposition and wafer-scale patterning as a means of producing nanohelices with significant yields: ~ 100 billion per deposition. This method has the distinct advantage that a wide variety of different materials can be used and combined with one another to form hybrid nanohelices as well as alloys. To demonstrate this versatility, we have fabricated Ag/Cu alloy nanohelices, cone-shaped helices, chiral plasmonic metamaterial arrays and nanoparticles, ferromagnetic nanohelices, as well as hybrid Au-nanodot decorated oxide nanohelices. Also the method allows for the combination of other geometries with the nanohelix such as straight rods and zigzag morphologies. The technique therefore allows for a wide range of applications with tailored optical, magnetic, and mechanical properties, nanoscale propulsion in fluids, and an a wide range of future applications yet to be explored.

Acknowledgements

We thank Conny Miksch and Joachim Spatz for help with the BCML and Eberhard Goering and Claudia Stahl for assistance with the magnetic SQUID measurements. This work was supported in part by the European Research Council under the ERC Grant Agreement No. 278213.

Notes

*email: fischer@is.mpg.de

^a Max Planck Institute for Intelligent Systems, Heisenbergstr. 3, 70569 Stuttgart, Germany.

^b Institute for Physical Chemistry, University of Stuttgart, Pfaffenwaldring 55, 70569 Stuttgart, Germany.

† Part of the Nanoscale themed issue on "Helical Micro- and Nanostructures"

References

1. H. Nakano, H. Takeda, Y. Kitamura, H. Mimaki and J. Yamauchi, *Antennas and Propagation, IEEE Transactions on*, 1992, 40, 279-284.
2. L. Novotny and N. van Hulst, *Nature Photonics*, 2011, 5, 83-90.

3. W. Hol, P. T. Van Duijnen and H. Berendsen, *Nature*, 1978, 273, 443.
4. M. Blaber, X.-J. Zhang and B. W. Matthews, *Science*, 1993, 260, 1637-1640.
5. J. M. Scholtz and R. L. Baldwin, *Annual review of biophysics and biomolecular structure*, 1992, 21, 95-118.
6. J. D. Watson, *The double helix: A personal account of the discovery of the structure of DNA*, Scribner, 2011.
7. P.-X. Gao and G. Liu, in *Three-Dimensional Nanoarchitectures*, Springer, 2011, pp. 167-204.
8. M. Yang and N. A. Kotov, *Journal of Materials Chemistry*, 2011, 21, 6775-6792.
9. P. X. Gao, Y. Ding, W. Mai, W. L. Hughes, C. Lao and Z. L. Wang, *Science*, 2005, 309, 1700-1704.
10. Y. Qiao, Y. Lin, Y. Wang, Z. Yang, J. Liu, J. Zhou, Y. Yan and J. Huang, *Nano letters*, 2009, 9, 4500-4504.
11. C. Li, K. Deng, Z. Tang and L. Jiang, *Journal of the American Chemical Society*, 2010, 132, 8202-8209.
12. J. Li, S. Sattayasamitsathit, R. Dong, W. Gao, R. Tam, X. Feng, S. Ai and J. Wang, *Nanoscale*, 2013.
13. L. Liu, S.-H. Yoo, S. A. Lee and S. Park, *Nano letters*, 2011, 11, 3979-3982.
14. Y. Wu, G. Cheng, K. Katsov, S. W. Sides, J. Wang, J. Tang, G. H. Fredrickson, M. Moskovits and G. D. Stucky, *Nature materials*, 2004, 3, 816-822.
15. A. Kuzyk, R. Schreiber, Z. Fan, G. Pardatscher, E.-M. Roller, A. Högele, F. C. Simmel, A. O. Govorov and T. Liedl, *Nature*, 2012, 483, 311-314.
16. A. G. Mark, J. G. Gibbs, T.-C. Lee and P. Fischer, *Nature materials*, 2013, 12, 802-807.
17. N. O. Young and J. Kowal, *Nature*, 1959, 183, 104-105.
18. M. T. Taschuk, M. M. Hawkeye and M. J. Brett, *Handbook of Deposition Technologies for Films and Coatings, 3rd ed.*(Elsevier, 2010), 2010, 621-678.
19. K. Robbie and M. Brett, *Journal of Vacuum Science & Technology A: Vacuum, Surfaces, and Films*, 1997, 15, 1460-1465.
20. Y.-P. Zhao, D.-X. Ye, G.-C. Wang and T.-M. Lu, *Nano Letters*, 2002, 2, 351-354.
21. M. M. Hawkeye and M. J. Brett, *Journal of Vacuum Science & Technology A: Vacuum, Surfaces, and Films*, 2007, 25, 1317-1335.
22. D. Vick, L. Friedrich, S. Dew, M. Brett, K. Robbie, M. Seto and T. Smy, *Thin Solid Films*, 1999, 339, 88-94.
23. B. Dick, M. Brett and T. Smy, *Journal of Vacuum Science & Technology B: Microelectronics and Nanometer Structures*, 2003, 21, 23-28.
24. H.-H. Jeong, A. G. Mark, J. G. Gibbs, T. Reindl, U. Waizmann, J. Weis and P. Fischer, *in preparation*, 2014.
25. I. Hodgkinson and J. Hazel, *Applied optics*, 1998, 37, 2653-2659.
26. R. Tait, T. Smy and M. Brett, *Thin Solid Films*, 1993, 226, 196-201.
27. K. Okamoto, T. Hashimoto, K. Hara and E. Tatsumoto, *Journal of the Physical Society of Japan*, 1971, 31, 1374-1379.
28. L. Abelmann and C. Lodder, *Thin Solid Films*, 1997, 305, 1-21.
29. M. Volmer, *Zeitschrift für Physik A Hadrons and Nuclei*, 1921, 5, 31-34.
30. A. Van der Drift, *Philips Res. Rep.*, 1967, 22, 267-288.
31. G. K. Larsen, Y. He, J. Wang and Y. Zhao, *Advanced Optical Materials*, 2014.
32. J. H. Singh, G. Nair, A. Ghosh and A. Ghosh, *Nanoscale*, 2013, 5, 7224-7228.
33. G. Nair, H. Singh, D. Paria, M. Venkatapathi and A. Ghosh, *The Journal of Physical Chemistry*, 2014.
34. J. Gibbs, A. Mark, S. Eslami and P. Fischer, *Applied Physics Letters*, 2013, 103, 213101.
35. J. K. Gansel, M. Latzel, A. Frolich, J. Kaschke, M. Thiel and M. Wegener, *Applied Physics Letters*, 2012, 100, 101109-101109-101103.
36. V. R. Coluci, A. F. Fonseca, D. S. Galvao and C. Daraio, *Physical review letters*, 2008, 100, 086807.
37. D. Liu, D. Ye, F. Khan, F. Tang, B. Lim, R. Picu, G. Wang and T. Lu, *Journal of Nanoscience and Nanotechnology*, 2003, 3, 492-495.
38. J. Happel and H. Brenner, *Low Reynolds number hydrodynamics: with special applications to particulate media*, Springer, 1965.
39. Z. Fan and A. O. Govorov, *Nano letters*, 2010, 10, 2580-2587.
40. M. Hentschel, M. Schaferling, T. Weiss, N. Liu and H. Giessen, *Nano letters*, 2012, 12, 2542-2547.
41. Z. Li, Z. Zhu, W. Liu, Y. Zhou, B. Han, Y. Gao and Z. Tang, *Journal of the American Chemical Society*, 2012, 134, 3322-3325.
42. J. Pendry, *Science*, 2004, 306, 1353-1355.
43. S. Link, Z. L. Wang and M. A. El-Sayed, *The Journal of Physical Chemistry B*, 1999, 103, 3529-3533.
44. A. O. Govorov, *The Journal of Physical Chemistry C*, 2011, 115, 7914-7923.
45. E. Hendry, T. Carpy, J. Johnston, M. Popland, R. Mikhaylovskiy, A. Laphorn, S. Kelly, L. Barron, N. Gadegaard and M. Kadodwala, *Nature nanotechnology*, 2010, 5, 783-787.
46. G. Nair, H. J. Singh, M. Venkatapathi and A. Ghosh, *Proc. of SPIE* 2014, 8994, 1-6.
47. F. Liu, M. Umlor, L. Shen, J. Weston, W. Eads, J. Barnard and G. Mankey, *Journal of applied physics*, 1999, 85, 5486-5488.
48. B. Dick, M. Brett, T. Smy, M. Freeman, M. Malac and R. Egerton, *Journal of Vacuum Science & Technology A: Vacuum, Surfaces, and Films*, 2000, 18, 1838-1844.
49. Y. He, J. Fu, Y. Zhang, Y. Zhao, L. Zhang, A. Xia and J. Cai, *Small*, 2007, 3, 153-160.
50. C. Phatak, Y. Liu, E. B. Gulsoy, D. Schmidt, E. Schubert and A. Petford-Long, *Nano letters*, 2014.
51. H. Schmidt and R. Ram, *Journal of Applied Physics*, 2001, 89, 507-513.
52. L. Lopez-Diaz, J. Rothman, M. Klaui and J. Bland, *Journal of Applied Physics*, 2001, 89, 7579-7581.
53. E. Lauga, *Physical review letters*, 2011, 106, 178101.
54. P. Mandal and A. Ghosh, *Physical Review Letters*, 2013, 111, 248101.
55. A. Ghosh and P. Fischer, *Nano letters*, 2009, 9, 2243-2245.
56. P. Fischer and A. Ghosh, *Nanoscale*, 2011, 3, 557-563.
57. D. Schamel, M. Pfeifer, J. G. Gibbs, B. r. Miksch, A. G. Mark and P. Fischer, *Journal of the American Chemical Society*, 2013, 135, 12353-12359.
58. A. Ghosh, D. Paria, G. Rangarajan and A. Ghosh, *The Journal of Physical Chemistry Letters*, 2013.

59. B. J. Nelson, I. K. Kaliakatsos and J. J. Abbott, *Annual review of biomedical engineering*, 2010, 12, 55-85.
60. A. Masuda, K. Ushida, H. Koshino, K. Yamashita and T. Kluge, *Journal of the American Chemical Society*, 2001, 123, 11468-11471.
61. S. De Smedt, A. Lauwers, J. Demeester, Y. Engelborghs, G. De Mey and M. Du, *Macromolecules*, 1994, 27, 141-146.
62. Q. Xu, N. J. Boylan, J. S. Suk, Y.-Y. Wang, E. A. Nance, J.-C. Yang, P. J. McDonnell, R. A. Cone, E. J. Duh and J. Hanes, *Journal of Controlled Release*, 2013, 167, 76-84.
63. J. Kirch, A. Schneider, B. Abou, A. Hopf, U. F. Schaefer, M. Schneider, C. Schall, C. Wagner and C.-M. Lehr, *Proceedings of the National Academy of Sciences*, 2012, 109, 18355-18360.